Coupled Level-Set/Volume-of-Fluid Method for the Simulation of Liquid Atomization in Propulsion Device Injectors

Marco Arienti[1], Xiaoyi Li[2], Marios C. Soteriou[3], Christopher A. Eckett,[4]
United Technologies Research Center, East Hartford, Conn. 06108

Mark Sussman[5]
Florida State University, Tallahassee, Fla. 32312

and

Robert Jensen[6]
Pratt & Whitney Rocketdyne, Canoga Park, Calif. 91309

This paper presents results of a multiphase computational fluid dynamics code utilizing a coupled level-set/volume-of-fluid method to simulate liquid fuel atomization. The coupled approach combines the mass conservation properties of the volume-of-fluid (VOF) method with the accurate surface reconstruction properties of the level-set (LS) method, and includes surface tension as a volume force calculated with second-order accuracy. The multiphase code builds upon a methodology developed by Sussman et al. [1] which enables bubbly flow, liquid breakup, and phase change simulations. Extensions to the model presented in this paper include coupling to a Lagrangian dispersed phase model for post-breakup tracking of droplets and multiple level-sets for tracking of surfaces and droplets of multiple species. Two simulations of like-on-like jet impingement of relevance to liquid rocket engine combustion are presented here, at low and high injection velocity, with comparison to validation data. Also shown is the first-ever demonstration simulation of unlike impinging jets.

---

[1] Staff Engineer, Thermal & Fluid Sciences Department, MS 129-29, Senior AIAA member
[2] Senior Engineer, Thermal & Fluid Sciences Department, MS 129-29, AIAA member
[3] Fellow of Research, Thermal & Fluid Sciences Department, MS 129-29, Senior AIAA member
[4] Principal Engineer, Pratt & Whitney Program Office, MS 129-88, Senior AIAA member
[5] Associate Professor, Department of Mathematics
[6] Associate Fellow, MC RQB-60, Senior AIAA Member

Nomenclature

α = drop sphericity

β = spray concentration

f_a = atomization frequency: $f_a = v_{jet}/\Delta l$

Δl = ligament spacing

l_j = jet pre-impingement length

m = Δx multiple of critical radius

R_{cri} = critical drop radius for Lagrangian transformation

Re = $\rho_l v_{jet} d_0/\mu_l$ Reynolds number based on liquid properties

V_L = blob volume

V_{cri} = critical drop volume for Lagrangian transformation

We = $\rho_l v_{jet}^2 d_0/\sigma$ Weber number based on liquid properties

I. Introduction

Impinging jet injectors rely on the mutual impact of two or more high-velocity jets to atomize the propellants. The elements may flow either a single propellant (like impinging) or fuel and oxidizer (unlike impinging), and typical geometries involve two, three or five streams (from doublet, triplet and pentad elements). This impingement results in a highly directional distribution of propellant(s) that must be managed to provide good mixing efficiency and combustor wall thermal compatibility. In the case of the doublet element, the distribution is that of a "fan" of pre-atomized liquid material which is at right angles to the common plane of the two liquid streams. For like impinging doublets, these fans must be interwoven in the overall injection pattern to insure sufficient mixing of fuel and oxidizer. Injection velocity and stream diameter control the droplet size distribution. The fans break up in various modes, but usually exhibit waves that separate into liquid ligaments in the plane of the fan [2]. These ligaments then fracture into droplets typically through Rayleigh breakup.

Because the atomization and mixing processes of such injectors are complex and strongly three-dimensional, impinging injector sprays have mainly been characterized experimentally, like most other similar atomization systems [3, 4]. An example is the study carried out at the United Technology Research Center (UTRC) High

Pressure Spray Facility [5], where the effects of liquid properties and chamber conditions on the spray characteristics were investigated using a Malvern Droplet Size Analyzer. Reynolds numbers were between $7.3 \cdot 10^4$ and $8.4 \cdot 10^4$ for the oxidizer and between $1.7 \cdot 10^4$ and $1.9 \cdot 10^5$ for the fuel. Photographs of the injection displayed the two jets crossing each other's path at the impinging point and forming quite a dense spray in the streams plane, suggesting a loss of cohesion of the streams before contact. Drop sizes from an Aerometrics Phase Doppler Particle Analyzer (PDPA) were found to decrease with increasing liquid flow rate, decreasing surface tension and increasing chamber density.

The formation of a liquid sheet which ruptures in increasingly less coherent ligaments with higher jet velocity has been described in impinging water jets experiments by Anderson et al. [6] and Ryan et al. [7]. In their study, from now on referred to with the acronym AR for ease of notation, the Weber number was increased from 350 to 6,600, with Reynolds numbers between $2.8 \cdot 10^3$ and $2.6 \cdot 10^4$. The measured breakup length along the centerline in that study showed a strong dependence on the turbulent condition of the jet at injection. In the turbulent case, the decrease of the core breakup length and the ligament frequency was correlated with the stability parameter d_0/v_{jet}. These data, as well as the average distance between adjacent ligaments and the PDPA characterization of the spray fan, are used for validation purposes in the work presented here.

Recently, interface capturing simulation techniques have been applied to simulate the primary atomization of impinging jets. In a set-up similar to the AR experiment, Inoue et al. [8, 9] used a cubic-interpolated propagation hybrid level set method (CIP-LSM) and a multi-interface advection and reconstruction solver (MARS) technique to capture the liquid surface and show the formation of the characteristic fan-shaped sheet. The sheet appeared to rapidly develop a flapping mode leading to its breakup. While the calculations [8, 9] were based on a fixed, orthogonally stretched computational grid, Li et al. [10] demonstrated the effectiveness of coupling the Combined Level Set Volume of Fluid (CLSVOF) formulation [1] with the Lagrangian tracking of the spray on a dynamically adaptive, block-structured grid. This adaptive approach selectively enables high grid density at the liquid interface, therefore increasing the accuracy of the primary breakup calculation. High-density grid boxes are embedded in a coarser (compared to the scales of primary atomization) computational domain for the Lagrangian representation of the dilute spray.

Highlights of the numerical method are provided in the next Section. If the domain is sufficiently broad to include where spray measurements are actually taken, it becomes possible to carry out a validation study of jet

impingement atomization at the same conditions of the AR experiment. This comparison constitutes the main body of the paper for a low and a high injection velocity case. See Table 1.

Table 1. Simulated impinging spray conditions. Data on the third and fourth column are taken from the diagrams in [6]. The values of f_a in parenthesis are from the uncertainty bars shown in the same picture.

v_{jet} [m/s]	$d_0 / v_{jet} \cdot 10^{-4}$ [s]	x_b/d_0 [·]	f_a [Hz]	$x_{b,calc.}/d_0$ [·]	$f_{a,calc.}$ [Hz]
6.4	1	16±2	3,900 (2,000-4,800)	12.4±2	3,300
18.5	0.343	27.5±2	6,800 (5,700-8,000)	16	4,400-5,900

II. Numerical method

The description of the CLSVOF method can be found elsewhere [1], together with several validation studies. Briefly, the Navier-Stokes equations for incompressible flow of two immiscible fluids (such as liquid and gas) are written in terms of a smooth level set function ϕ, whose zero level represents the time-evolving interface. In addition to the evolution equation for ϕ, the transport equation for the cell liquid volume fraction (the volume-of-fluid function, F) is solved. The interface normals in the VOF reconstruction step are determined from the level set function. The volume fractions are then used with the normals to construct a volume preserving distance function ϕ. In this way, volume is preserved by implementing a ‘‘local’’ mass fix at every iteration. Second-order accurate curvature is calculated from F by the method of height fraction. The Navier-Stokes equations are solved with the one-fluid approach, that is, the properties of density and dynamic viscosity are function of ϕ everywhere in the computational domain. Finally, velocity extrapolation based on ϕ from the liquid phase is used to approach the solution of the corresponding one-phase method in the limit of uniform gas pressure at large liquid-to-gas density ratios.

With adaptive mesh refinement (AMR), the cells that are crossed by the liquid-gas interface are tagged for refinement. Starting from the base level, boxes (with a minimum size of, say, 32^3 cells) are combined to cover all the tagged cells within assigned coverage efficiency. This set of blocks with the same grid spacing forms level 1. This level is in turn tagged for refinement at the interface, and the process is repeated until the input grid resolution is achieved. During the simulation, the data on the fine level are either copied from a previous time step or, when the

grid structure has changed locally, conservatively interpolated from the underlying coarse level. The interface, however, is always embedded in the finest grid level to avoid gross interpolation errors. In a time step, the calculation is carried out on all levels, and the updated data on a fine level are averaged to the underlying coarser one. For a given minimum grid spacing, a higher granularity of the coverage (i.e., the prescription of many small AMR boxes) minimizes the grid count but maximizes data communication between boxes, and vice-versa. Assuming the optimal coverage closely follow the interface, it is reasonable to estimate that doubling the grid density in a three-dimensional simulation corresponds to increasing the storage and the execution time by a 2^3 factor, instead of the 2^4 factor (three dimensions plus time) required by a grid without AMR. This saving in resources is repeated at every new refinement level.

Following the approach by Herrmann [11], droplets in dilute spray regions are converted into Lagrangian particles. Because such droplets are removed from the Eulerian description, in the region interested by the transformation the hierarchy of refinement levels quickly reverts to the underlying base level. Thus, the grid refinement remains localized to a small volume around the jet, and the simulation cost can be eased by a relatively coarse grid far from injection.

The removal of liquid structures from the Eulerian description is based on criteria of droplet size, sphericity and local droplet concentration, as described in [10]. The volume of a candidate liquid structure is constrained to be less or equal to a critical value,

$$V_L \le V_{cri} = \frac{4}{3}\pi R_{cri}^3, \tag{1}$$

where $R_{cri} = m\,\Delta x$ and m is a user-prescribed small integer. If the droplet is small enough, further breakup (referred to as secondary breakup) cannot occur due to the high surface tension compared to the aerodynamic force. In the calculations, the Weber number of the Lagrangian particles is monitored at each time step, and this diagnostics confirms the absence of the conditions for secondary breakup in the simulations presented here.

A second criterion is the droplet sphericity, defined as

$$\alpha = \frac{R_{max}}{\max\left[\Delta x, \left(\frac{3}{4\pi}V_L\right)^{1/3}\right]}, \tag{2}$$

where R_{max} is the maximum distance from the center of mass of the liquid blob of a cell centroid, and V_L is the blob volume. Largely deformed blobs are more probable to experience further break-up, which should be captured in the Eulerian representation. So we ensure that the transformation can occur only when $\alpha \leq \alpha_{cri}$.

A maximum local spray concentration β_{cri} is also defined, below which the transformation to the Lagrangian phase can occur. The local concentration is defined as the ratio of the total liquid volume in an AMR box to the volume of the box. For the cases examined in the following Section, we observed limited sensitivity of the results to variations of this parameter if $\beta_{cri} \sim 0.01$. The values used in this work are $m = 4$ and $\alpha_{cri} = 2$.

The Lagrangian trajectories of the particles are tracked on the base grid flow velocity using a simple drag model [12].

III. Results

The AR experiment used precision bore glass tubes to minimize the effects of surface roughness, with internal diameter $d_0 = 0.635$ mm. The impingement angle was 60° and the pre-impingement length $l_j = 25.4$ mm. The PDPA measurements at the spray fan centerline were taken 16 and 41 mm downstream of the impingement point. The PDPA optical configuration was set to provide a 40 to 1,400 μm range of drop diameters. The test liquid was water ($\rho_l = 998$ kg/m^3, surface tension $\sigma = 0.076$ N/m, and dynamic viscosity $\mu_l = 0.0010$ kg/m/s). The breakup length, from the impingement point to the perceived breakup of the intact sheet, and the distance between adjacent ligaments were estimated as averages extracted from 17 instantaneous images of the spray field, each image taken with a diffuse strobe light and time duration of 5 μs.

A snapshot of the simulation is shown in Figure 1, including the rendered zero level set iso-surface and the Lagrangian droplets (in lighter color). In the plot, these point-like particles are given a spherical shape and rendered with their effective diameter. Injection occurs in the *y*-*z* plane, with the *z* axis aligned in the common direction of the two jets. To reduce the overall size of the computational domain, the bottom plane (at $z = 0$) is not the injection wall of the experiment, but rather truncates the two liquid columns at the pre-impingement length $l_j = 4$ mm. Outflow boundary conditions are enforced on all the other planes. The injection velocity consists of a plug flow profile, without inner turbulence effects. While the effects of injection turbulence should be examined in more detail, the exclusion of its effects isolates the role of fluid dynamic instability in sheet breakup. The overall box size is 16 by 12 by 24 mm, and droplets are sampled at a plane 16 mm past the impingement point.

Figure 1. Isometric view of the impinging jets.

A. Low- velocity injection case

The injection velocity in this case is v_{jet} = 6.4 m/s. In Figure 2, the snapshot side view of the liquid sheet past the impingement (left) can be compared with a snapshot of the experiment (right) at the same conditions and on the same length scale. The calculation is carried out with two levels of refinement, corresponding to a minimum grid spacing of 31.25 μm. In both pictures, waves propagate radially from the impingement point, with tears along the intact sheet that deepen until they detach thin ligaments from the periphery of the sheet. The rendered zero level set iso-surface in Figure 2a does not actually provide a sense of the thickness of the sheet, but further inspection and the comparison with snapshots from the experiment reveals the existence of very thin membranes, where tearing initiates, and of thicker crests between them.

It can be expected that a breakup length based on the perception of continuity of the liquid sheet is strongly dependent on the capability by the interface-capturing algorithm of resolving a very thin membrane. The measured sheet breakup length reported in the AR paper was 10 mm, with standard deviation of ±2.5 mm. The average length estimated from 12 simulation snapshots is 7.9 ±1 mm. This value is at the low end of the range of measured sheet breakup lengths.

The atomization frequency in the AR results was defined as the ratio of sheet velocity to the spacing of detached ligaments. Since the maximum ligament spacing found from the calculation snapshots is 1.9 mm, the corresponding frequency, 3,400 Hz, falls well within the error band reported for this injection velocity.

The ligaments fracture rather quickly after forming, and their fragments equilibrate into almost spherical droplets that carry the residual momentum of the jet. The largest drops can be found near the centerline of the fan, while smaller droplets are located at its periphery. Because of the parameters used in the simulation ($\beta_{cri} \sim 0.01$; $m = 4$; $\alpha_{cri} = 2$), several droplets near the centerline are never switched to Lagrangian particles.

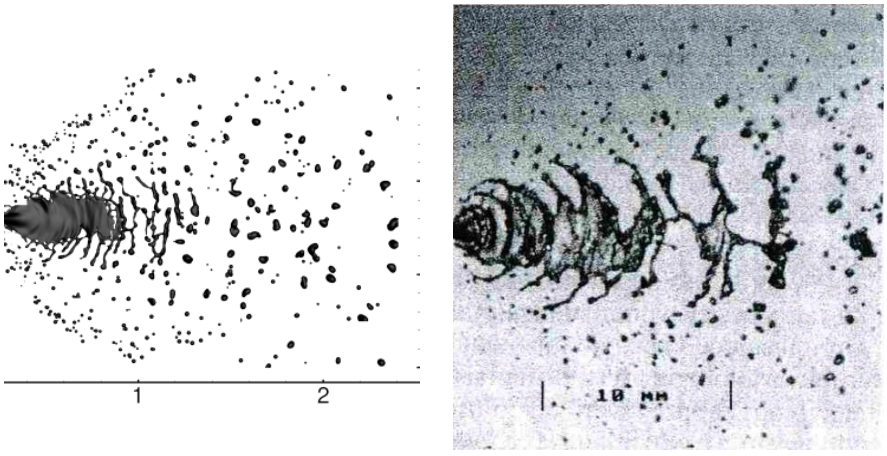

(a) (b)

Figure 2. Low-velocity injection case. A side view of the liquid sheet past the impingement point is shown.

B. High-velocity injection

The injection velocity in this case is v_{jet} = 18.5 m/s. A snapshot side view of the liquid sheet past the impingement point is shown in Figure 3, where calculation with decreasing Δx_{eff} (the minimum Δx from the given number of refinement levels) in frames (a), (b), and (c) can be compared with a snapshot of the experiment at the same conditions and on the same length scale in frame (d). The calculation in frame (a) shows a very modest liquid sheet and almost no ligaments, substituted by the large spherical particles of their Lagrangian representation. It can be argued that such a low grid resolution is insufficient to capture the basic atomization mechanism of sheet formation and breakup. The addition of a refinement levels leads to a substantial improvement in the appearance of the liquid sheet, which is now longer and broader. To give an idea of the computational cost involved, at the steady-

state conditions where the snapshot was taken the central processor unit (CPU) time was approximately 150 seconds per time step (Δt = 0.66 μs) on two 8-core, 32 Gb, 3,000 MHz nodes with InfiniBand switch. By adding one more refinement level, the appearance of the calculation still evolves and reveals longer and more arched ligaments. However, the droplet sizes near the measurement plane, at the right-hand side of the plots, appear very similar in frames (b) and (c). This suggests that, as far as the far-field spray is concerned, the size distribution could be approaching convergence. This outcome is confirmed by the following analysis.

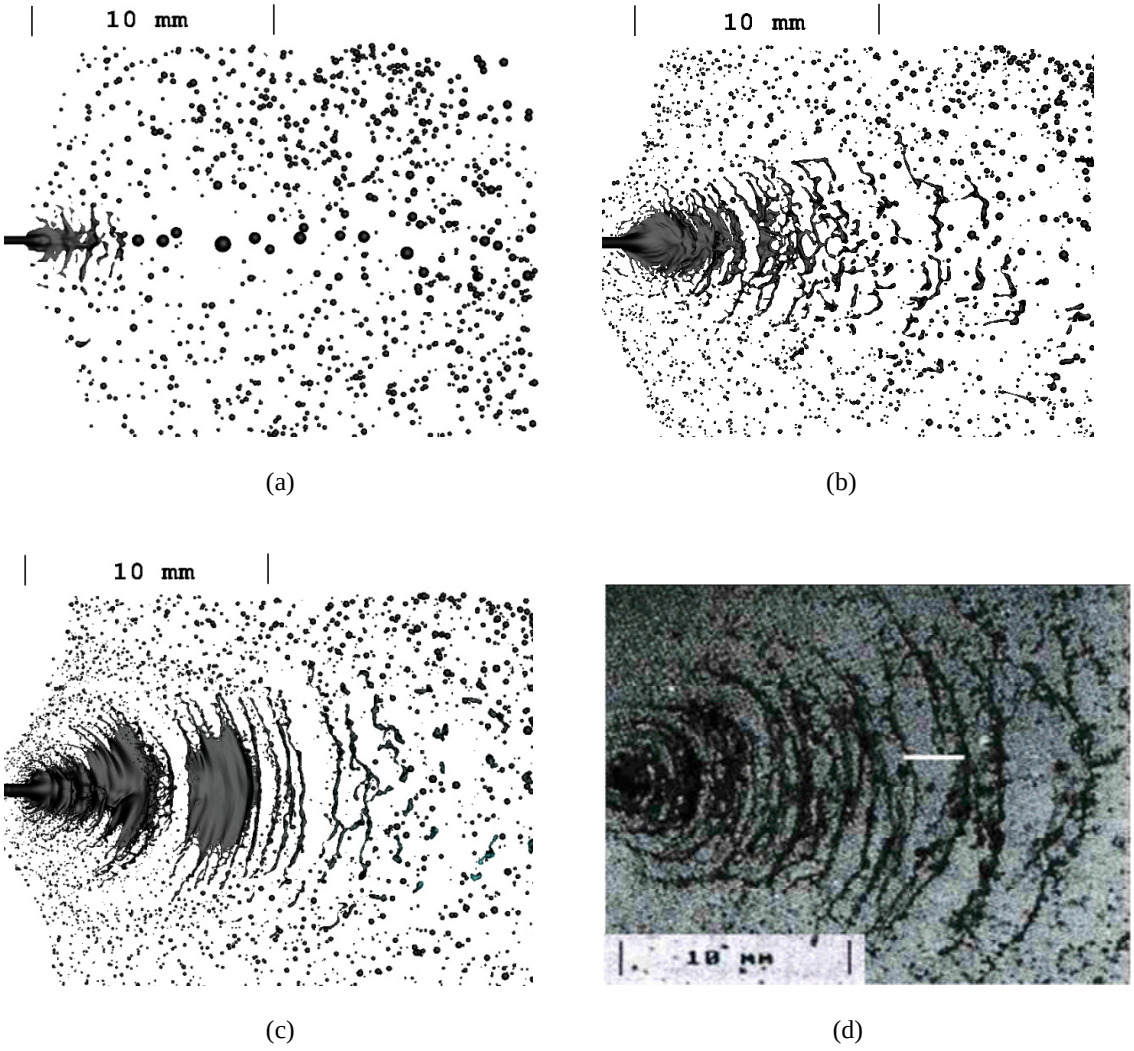

(a) (b)

(c) (d)

Figure 3. High-velocity injection case. Side view snapshots of the simulation are shown with (a) minimum Δx = 62.5 μm (1 level of refinement), (b) Δx = 31.25 μm (2 levels of refinement) and (c) Δx = 15.625 μm (3 levels of refinement). Frame (d) is a snapshot of the AR experiment at the same injection condition.

In Figure 4, the normalized histograms of droplet size distribution at the center of the z = 20 mm sampling plane are compared with the PDPA measurements at z = 41 mm from [6]. The three frames in the figure correspond to the three refinement levels discussed above. As expected, the droplets resulting from the coarsest simulation are too large, peaking at around 200 μm, whereas the distributions in frames (b) and (c) are in good agreement with the data. In frame (b), droplets were sampled between 5.24 and 6.58 ms to exclude initial startup effects, for a total of 1086 samples. A lower number of samples (480) is currently available for the highest resolution calculation in frame (c).

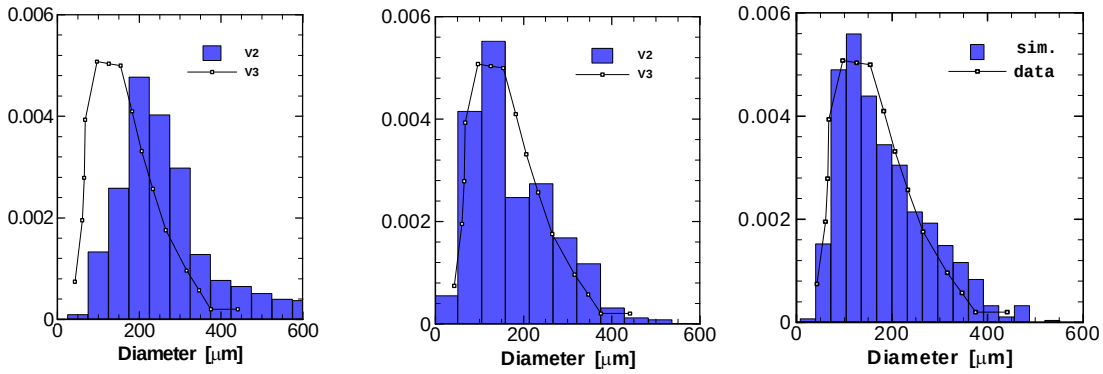

(a) (b) (c)

Figure 4. High-velocity injection. Comparison of the density distribution of droplet size from the AR experiment (symbols) and from the simulation: (a) 1 level of refinement with minimum Δx = 62.5 μm; (b) 2 levels of refinement with minimum Δx = 31.25 μm; (c) 3 levels of refinement with minimum Δx = 15.625 μm.

Compared to the low-velocity case, the ligaments still display a somewhat regular spacing near the core, whereas droplets tend to disperse in an apparently more disorganized pattern in the far field. To establish whether the spray flow rate exhibits any natural coherence, the field pressure was monitored at z = 8 mm (Probe 1) and z = 10 mm (Probe 2) along the spray centerline. The resulting pressure time history, shown in Figure 5, registers an increase in gauge pressure every time a liquid element crosses the probe point. The sequence of peaks in the two plots is somewhat irregular, but still suggests a periodicity that is best revealed by the Fast Fourier Transform (FFT) of the two signals, displayed in Figure 6. The largest peak for Probe 1 is found at 5,900 Hz, whereas the largest peak for Probe 2 is at 4,400 Hz. These two values are at the lower end of the 6,000 to 8,000 Hz range that is reported for

atomization frequency. Based on the average value of this range and on the injection jet velocity, one finds a value of ligament spacing of 2.6 mm. This length is marked as a white segment on the experiment snapshot of Figure 3d.

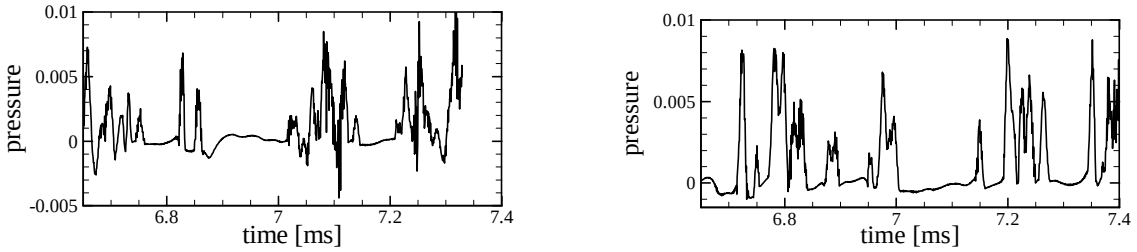

(a) (b)

Figure 5. Pressure time history at two centerline locations past film breakup: *z* = 8 (a) and *z* = 10 mm (b).

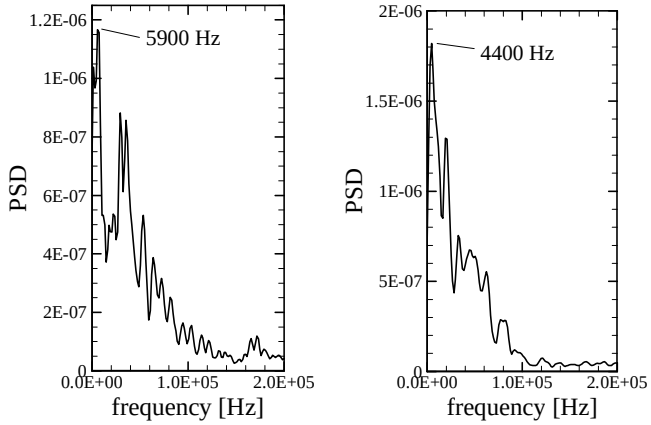

(a) (b)

Figure 6. FFT of the two pressure signals of the high-velocity AR experiment at *z* = 8 (a) and *z* = 10 mm (b). The sampling frequency is $1.5 \cdot 10^6$ Hz.

Concluding the results analysis is a consideration on the predicted breakup length of the sheet. The AR value is 17.5 mm, almost twice the length of the low-velocity injection case, with an uncertainty band of ±2.5 mm. On the snapshot of Figure 3d, the sheet extends from the impingement point for about two thirds of the field of view, spanning what could possibly be disconnected ligaments. Based on the same criterion, the intact sheet length from

the calculation increases to 10, possibly 11 mm at the highest grid resolution. These values are at the low end of the AR uncertainty band, and this is encouraging, considering the somewhat subjective nature of the estimated length.

IV. Remarks and conclusion

The apparent periodic nature of liquid sheet breakup suggests a form of fluid dynamic instability. The linear temporal stability analysis by Dombroski and Johns [13] – as applied to a thinning, two dimensional viscous liquid sheet – leads to a quadratic dispersion relation including surface tension and aerodynamic forces.

High-fidelity calculations can assist in the analysis by providing a reference thickness and sheet velocity. In examining slices cut along the mid-plane of the computational domain, the sheet velocity appears remarkably close to the injection value. See Figure 7. Also close are the thicknesses of the two cases – approximately 0.2 mm in the low-velocity case and 0.25 mm in the high-velocity case. Clearly visible are long waves (larger than thickness) sheet oscillations that could be linked to ligament formation. Estimates of sheet velocity and thickness from the simulations are sufficient to determine the most unstable wave length in the inviscid analysis of a constant thickness, infinite sheet undergoing a sinuous mode [14]. The values calculated at the nominal jet injection velocity and for the thicknesses reported above are 1.2 and 1.5 mm, for the low- and high- velocity case, respectively. While these values are smaller than the spacing reported in the AR papers as derived from the atomization frequencies on Table 1 (approximately 1.6 and 2.7 mm), they seem to capture the correct increasing trend with increasing injection velocity.

As the last result, a demonstration of two immiscible liquid jets (water and oil) impinging at 60° is shown in Figure 8. As it is apparent from the bottom row of the figure, the lower momentum of the oil – since the injection velocities are the same and ρ_{oil} = 910 kg/m^3 – causes the tilting of the spray fan away from the water side. The droplet penetration to the far side of the opposing species illustrates the mixing potential of such atomizers. Whether waves develop in the spray fan similar to those in the like-on-like case needs to be further investigated.

Computationally, this calculation requires the simultaneous update of two independent sets of the level set and volume of fluid functions, as well as the tracking of the Lagrangian droplets for both liquids. In addition to the properties of the two liquids, the surface tension of one liquid with respect to the other needs to be input in the calculation. The values used in the calculation are σ_{water} = 72.6 mN/m, σ_{oil} = 28.2 mN/m, and $\sigma_{w\text{-}o}$ = 44.5 mN/m. Note that in this formulation the flow field of the gas phase is still included in the simulation. Also, without

modifications of the original CLSVOF algorithm, the sum of the volume fraction of the two liquids is found to be bounded by unity with good approximation. To the author's knowledge, this is the first demonstration of such multi-material capability in the spray modeling area.

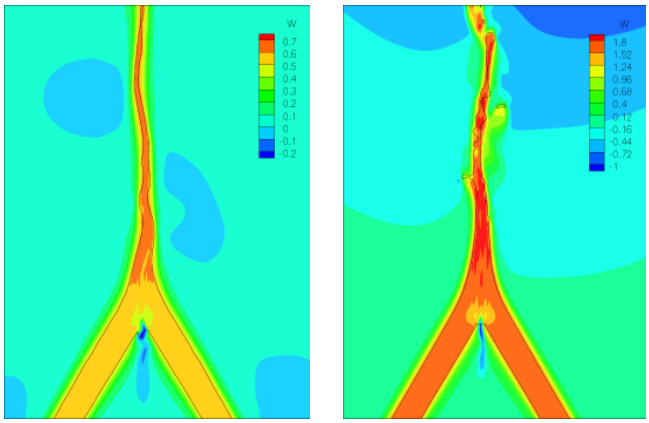

(a) (b)

Figure 7. Contour plot of vertical velocity along the center plane slice for the low- and high-injection velocity cases (frames (a) and (b), respectively). Velocities are normalized by 10 m/s.

This case concludes for the moment the description of the effort in applying the CLSVOF methodology as a tool for predicting impinging spray atomization, through addition of new physics and its validation. Extensions presented in this paper include coupling to a Lagrangian dispersed phase model for post-breakup tracking of droplets, and multiple level-set / volume-of-fluid functions for tracking of surfaces from multiple species. So far, the salient features of the spray fan breakup and ligament frequencies have shown agreement with both the trends and magnitudes of the corresponding experimental results.

Acknowledgments

The authors would like to extend their gratitude to United Technologies Research Center and Pratt and Whitney Rocketdyne for support and funding. Performance optimization that enabled this work used resources of the National Energy Research Scientific Computing Center, which is supported by the Office of Science of the U.S. Department of Energy under Contract No. DE-AC02-05CH11231.

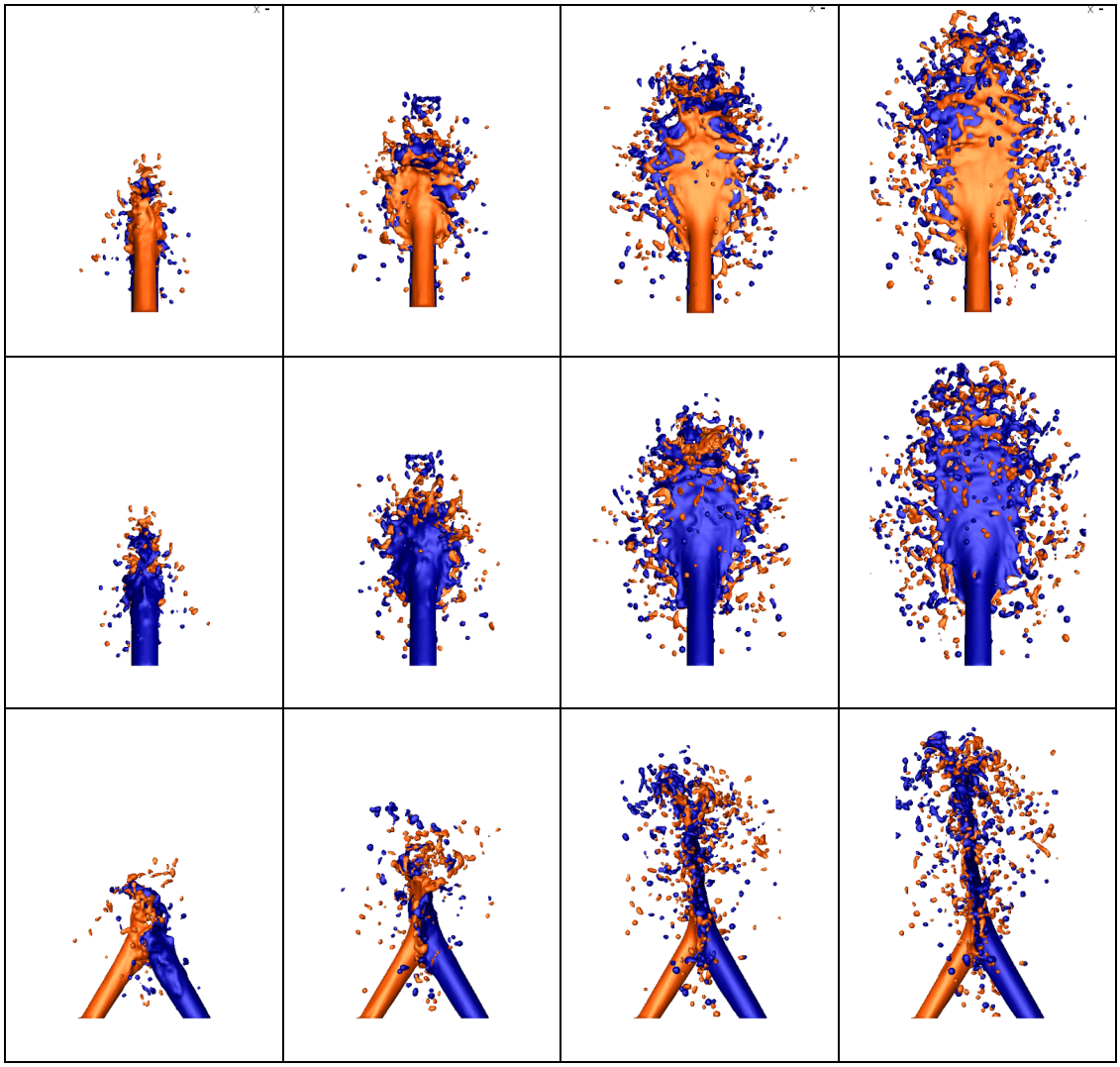

Figure 8. Two jets of immiscible liquids – water (blue) and oil (orange) – impinging at the same velocity with 60° angle.

References

[1] Sussman, M., Smith, K. M., Hussaini, M. Y., Ohta, M., and Zhi-Wei, R., "A Sharp Interface Method for Incompressible Two-Phase Flows," *Journal of Computational Physics*, v. 221, 2007.

[2] Tanasawa, Y., Sasaki, S., and Magai, N., "The Atomization of Liquids by Means of Flat Impingement," Technology Reports of the Tohoku University, 22, 1957.

[3] Sirignano, W. A., "Fluid Dynamics and Transport of Droplets and Sprays," Cambridge University Press, 1999.

[4] Ferrenberg, A., "Atomization and Mixing Study, Final Report," NASA Contract NAS8-34504, 1985.

[5] Hautman, D. J., "Spray Characterization of Like-on-Like Double Impinging Rocket Injectors," AIAA 91-0687, 29th Aerospace Science Meeting, 1991.

[6] Anderson, W. E., Ryan, H. M., Santoro, R. J., and Hewitt, R. E., "Combustion Instability Mechanism in Liquid Rocket Engines Using Impinging Jet Injectors," 31st AIAA ASME SAE ASEE Joint Propulsion Conference, AIAA 95-2357.

[7] Ryan, H. M., Anderson, W. E., Pal, S., and Santoro, R. J., "Atomization Characteristics of Impinging Liquid Jets," *J. of Propulsion and Power*, 11(1) 135-145, 1995.

[8] Inoue, C., Watanabe, T., and Himeno, T., "Study on Atomization Process of Liquid Sheet Formed by Impinging Jets," 44th AIAA/ASME/SAE/ASEE Joint Propulsion Conference & Exhibit, Hartford, CT, AIAA 2008-4847 (2008).

[9] Inoue, C., Watanabe, T., and Himeno, T., "Liquid Sheet Dynamics and Primary Breakup Characteristics at Impingement Type Injector," 45th AIAA/ASME/SAE/ASEE Joint Propulsion Conference & Exhibit, Denver, Colorado AIAA 2009-5041 (2009).

[10] Li, X., Arienti, M., Soteriou, M., Sussman, M., "Towards an Efficient, High-Fidelity Methodology for Liquid Jet Atomization Computations", AIAA-2010-0210, 48th AIAA Aerospace Sciences Meeting 2010.

[11] Herrmann, M., "A parallel Eulerian interface tracking/Lagrangian point particle multi-scale coupling procedure," *Journal of Computational Physics*, 229(3) 745-759, 2010.

[12] Liu, A.B., Mather, D., and Reitz, R.D., "Modeling the effects of drop drag and breakup on fuel sprays," SAE Technical Paper 930072, SAE, 1993.

[13] Dobrowski, N. and Johns, W.R., "The Aerodynamic Instability and Disintegration of Viscous Liquid Sheets," *Chemical Engineering Science*, 18(3), pp. 203-214, 1963.

[14] Rangel, R.H., and Sirignano, W.A., "The linear and nonlinear instability of a fluid sheet," *Phys. of Fluids* 3(10), pp. 2392-2400, 1991.